PROCEEDINGS A

royalsocietypublishing.org/journal/rspa

Research

Check for updates

Cite this article: Tian Y-Z, Wang Y-F, Laude V, Wang Y-S. 2026 Acoustic Willis metasurface for perfect transmedia wave manipulation. *Proc. R. Soc. A* **482**: 20251021.
https://doi.org/10.1098/rspa.2025.1021

Received: 27 November 2025
Accepted: 22 May 2026

Subject Areas:
acoustics, wave motion, mathematical physics

Keywords:
Willis coupling, acoustic metasurface, transmedia transmission, perfect wave manipulation, impedance theory

Author for correspondence:
Yan-Feng Wang
e-mail: wangyanfeng@tju.edu.cn

Acoustic Willis metasurface for perfect transmedia wave manipulation

Yu-Ze Tian[1], Yan-Feng Wang[1,2], Vincent Laude[3] and Yue-Sheng Wang[1,4]

[1]School of Mechanical Engineering, Tianjin University, Tianjin 300350, People's Republic of China
[2]National Key Laboratory of Vehicle Power System, Tianjin 300350, People's Republic of China
[3]CNRS, Institut FEMTO-ST, Université Marie et Louis Pasteur, Besançon 25000, France
[4]Institute of Engineering Mechanics, Beijing Jiaotong University, Beijing 100044, People's Republic of China

Y-ZT, 0009-0005-8926-1956; Y-FW, 0000-0002-5646-4475; VL, 0000-0001-8930-8797; Y-SW, 0000-0002-0043-8411

Transmission of sound waves through the water–air interface is a critical question for acoustic communications. The significant contrast in the parameters of both media indeed results in a severe challenge for wave manipulation. In this paper, the concept of acoustic Willis metasurface is proposed for transmedia beam steering with complete transmission. Such a metasurface supplies arbitrary phase shifts together with perfect transmission in one dimension, by appropriate modulation of material parameters, owing to the presence of Willis coupling terms. A hybrid Willis coupling element is proposed as the unit structure of transmedia impedance metasurfaces. Impedance theory is first recalled for two-dimensional beam steering, and the relationship between impedance components and material parameters is then given explicitly. A two-step optimization process ensures independent cell design while mitigating transverse acoustic-structure interaction. As a result, perfect power flow manipulation through the water–air interface is achieved with extreme steering angle. The present

THE ROYAL SOCIETY PUBLISHING

work provides a new perspective for the application of Willis coupling materials and an alternative theoretical support for transmedia metasurface design.

1. Introduction

Sound waves constitute the dominant carrier for oceanic exploration and information transfer. Underwater acoustic systems have established a comprehensive communication network interfacing with submersible vehicles, mining apparatus and submarines [1,2]. However, direct contact with airborne devices remains impeded by the water–air interface [3], since the material parameters of water and air exhibit huge contrast [4]. In principle, for plane waves, less than 0.1% of acoustic power can be emitted through the interface between them [5].

The concept of metasurface provides a pioneering solution to this problem [6]. As a paradigmatic two-dimensional implementation of metamaterials [7], metasurface shows extraordinary functionality. Through precisely engineered sub-wavelength structures, reflective and refractive waves can be manipulated subjectively and passively [8]. For water–air sound transmission, a meta-screen comprising a single layer of bubbles was designed [9] inspired by the underwater air bubble scattering of acoustic waves [10–12]. From the perspective of multiple scattering theory, each excited bubble becomes a radiation source on the interface, allowing for emission of sound power into air. This idea was then improved with a bubble-embedded frame for better stability [13]. It was found that the operating frequency for efficient transmission can be adjusted by placing the frame at different depths underwater. Meanwhile, the high-order resonant modes of bubbles provide multi-band operation as well [14], but that the bandwidth is relatively narrow. A more direct solution was proposed [15] by paralleling bubbles with different geometries. The designed metasurface can be customized for wideband or multi-band operation. Moreover, some strategies conversely focused on the interaction between bubbles and the frame itself: the contribution of single-layer [16] or multi-layer [17] bubble-frame metasurfaces to transmedia transmission was analysed comprehensively.

Meanwhile, the problem of impedance matching in some bubble metasurfaces [13–15], adapted from electromagnetic transmission line theory, has attracted great attention. It can be proven that the intermediate medium should own a characteristic impedance equal to the geometric mean of the two media to be connected, in order to ensure the complete transmission of plane wave [18]. This solution was verified in numerical simulations using a composite waveguide with tunable characteristic impedance for water–air sound transmission [19]. However, the rigidity assumption of the solid part may not be rigorously achieved in practice. Hence, a membrane-mass metasurface within a cylindrical waveguide was then designed and verified experimentally [20]. The wall of the waveguide was thick enough to ensure the effectiveness of the rigidity assumption. Contrarily, taking advantage of structural vibration, lightweight discrete metasurfaces utilizing acoustic-structure interaction as the major mechanism can be designed [21,22], which leads to easier implementation. It should be mentioned that perfect power transmission in the case of homogeneous impedance adaption is accompanied by a fixed transmitted phase difference of quarter-wavelength [20]. A metasurface composed of a unit that is series-connected to multiple substructures could remove this constraint [23]. Each substructure owns its characteristic impedance, matching its neighbours, while at the same time providing additional degrees of freedom for arbitrary phase shifting. However, the neglect of transverse acoustic-structure interaction then results in unsatisfactory overall performance. Almost at the same time, another solution was suggested with the concatenation of two substructures that independently achieve amplitude and phase modulation [24]. The phase-shifting substructure is entirely placed in air and can be considered as rigid; the acoustic-structure interaction caused by phase gradients is therefore eliminated.

An alternative solution was given recently [25] based on transformation theory [26–31]. It was shown that amplitude and phase shifting of transmedia transmitted wave can be modulated simultaneously through transformation-induced Willis metamaterials. The Willis metamaterial was first raised by Willis in 1981 for the elastodynamics of inhomogeneous medium [32]. It was then developed for the design of a transformation-based elastic invisible cloak showing abnormal wave behaviour [29]. It can be regarded as an effective description of structures with directivity, which introduces additional degrees of freedom, thereby promoting sophisticated wave manipulation [33,34]. After the experimental validation of the feasibility of Willis metamaterials [35], practical structures have been proposed for both acoustics and elasticity. A meta-atom that suppresses thermoviscous losses was presented with strong Willis coupling [36]. The vectorial coupling strength can be adjusted by changing the size and direction of the openings [37]. The Willis metamaterial in elastodynamics was proposed by Milton using a mass-spring model [38]. The elastic Willis coupling constitutive relation is governed by a tensor that can be determined through mechanical analysis of the coupling element [39]. It has been demonstrated that Willis metasurfaces composed by such metamaterials could offer additional knobs for sound wave manipulation. However, there seems to be no solution yet for the design of hybrid Willis metasurfaces subject to acoustic-structure interaction.

In this paper, perfect acoustic transmedia wave manipulation is achieved by Willis metasurfaces. The mapping between the parameters of the Willis metamaterial and the corresponding interface impedance matrix is given explicitly. The coverage of an arbitrary phase difference in the range 0–2π with 100% transmittance is proven. Willis metasurfaces based on impedance theory are implemented showing nearly perfect transmedia wave manipulation. A hybrid structure with Willis coupling is proposed and its mechanical properties are analysed. A two-step optimization method is suggested for the design of Willis metasurfaces with minimal transverse acoustic-structure interaction. Two examples of transmedia Willis impedance metasurfaces, with small and large steering angles, are presented. Their performances are validated though numerical simulations.

2. Transmedia Willis metamaterial unit

The transmedia transmission model is established as shown in figure 1a. A and B are two general homogeneous acoustic media connected in series by a material with Willis coupling at planes $x_1 = 0$ and $x_2 = h_0$, respectively. The governing equations for the two general media read [40]

$$\begin{cases} -p = K\nabla \cdot \boldsymbol{u}, \\ \boldsymbol{\mu} = \rho \boldsymbol{v}, \\ \dot{\boldsymbol{\mu}} = -\nabla p, \end{cases} \tag{2.1}$$

where p is the sound pressure, $\boldsymbol{u}$ and $\boldsymbol{v}$ are the local displacement and the local velocity, respectively, $\boldsymbol{\mu}$ is the momentum density, ∇ is the gradient operator, ρ is the mass density, and K is the bulk modulus. The first line is the constitutive equation, while the second and third lines are the physical equations expressing momentum conservation. The equation can be rewritten as a time-harmonic Helmholtz form [41]

$$\nabla \cdot \left(\frac{1}{\rho_i}\nabla p\right) = -\frac{\omega_0^2}{K_i}p, \qquad i = A, B, \tag{2.2}$$

where ω_0 is the operating angular frequency. The local velocity field can be derived from it as

$$\boldsymbol{v} = \frac{\imath}{\omega_0 \rho_i}\nabla p, \quad i = A, B, \tag{2.3}$$

where $\imath$ is the imaginary unit. The characteristic impedance of each media can be calculated by [42]

$$Z_A = \sqrt{\rho_A K_A} \tag{2.4a}$$

and

$$Z_B = \sqrt{\rho_B K_B}. \tag{2.4b}$$

https://royalsocietypublishing.org/journal/rspa Proc. R. Soc. A 482: 20251021

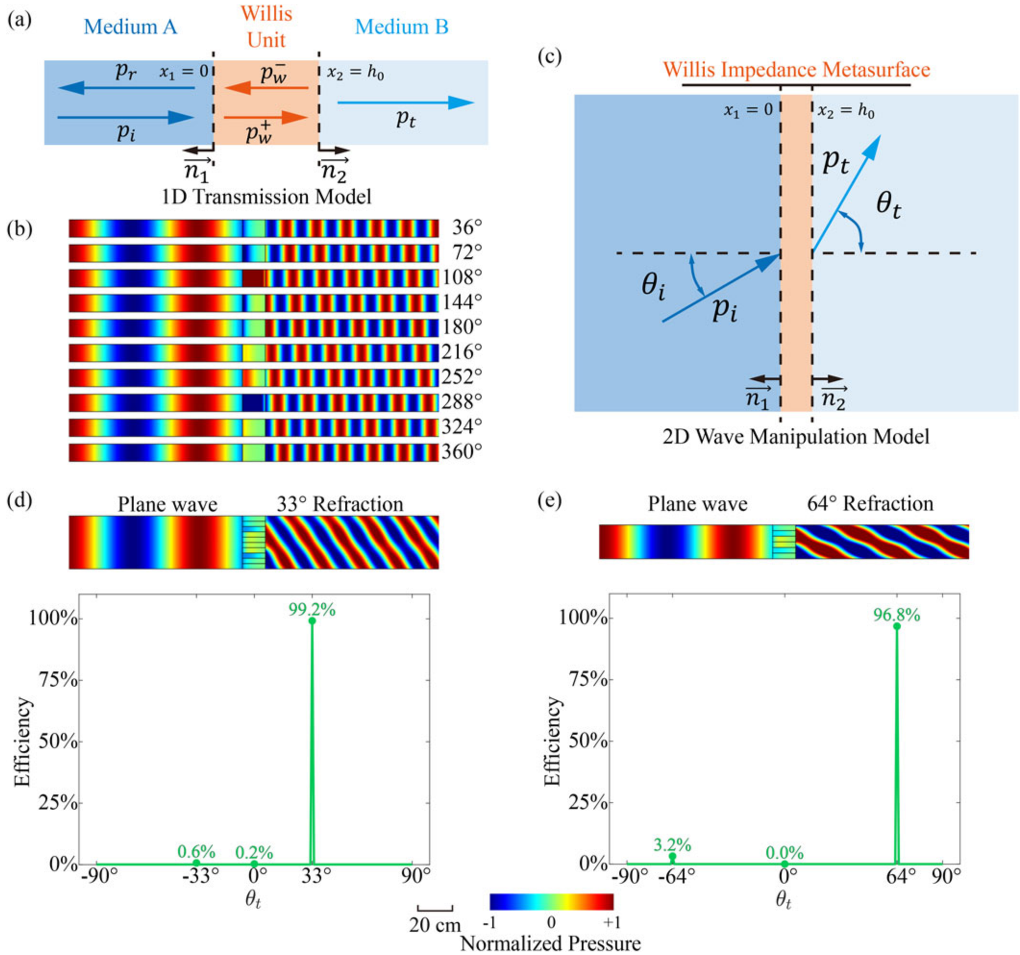

Figure 1. One-dimensional and two-dimensional transmedia wave manipulation by Willis metasurfaces. (a) One-dimensional transmedia transmission model. (b) Transmedia Willis units for phase shifting. (c) Schematic diagram of transmedia impedance metasurface. The responses of transmedia Willis impedance metasurfaces and corresponding quantitative evaluation by two-dimensional Fourier transform with an angle of refraction of (d) 33° and (e) 64°.

The material with Willis coupling shown in the middle of figure 1a is termed a Willis metasurface since its thickness is by design chosen as sub-wavelength. A pair of coupling terms depending on the acceleration and the velocity gradient is introduced in the governing equation as [37,43]

$$\begin{cases} -p = K_w \nabla \cdot \boldsymbol{u} + \boldsymbol{S}_w \cdot \dot{\boldsymbol{v}}, \\ \boldsymbol{\mu} = \boldsymbol{S}_w \nabla \cdot \boldsymbol{v} + \rho_w \boldsymbol{v}, \\ \dot{\boldsymbol{\mu}} = -\nabla p, \end{cases} \tag{2.5}$$

where ρ_w and K_w are the mass density and the bulk modulus of the Willis metamaterial, and $\boldsymbol{S}_w$ is its vectorial Willis coupling strength. Within the time-harmonic assumption, the governing equations can be simplified as

$$\begin{cases} -\imath\omega_0 p = K_w \nabla \cdot \boldsymbol{v} - \omega_0^2 \boldsymbol{S}_w \boldsymbol{v}, \\ -\nabla p = \imath\omega_0 \boldsymbol{S}_w \cdot \boldsymbol{v} + \imath\omega_0 \rho_w \boldsymbol{v}. \end{cases} \tag{2.6}$$

For this one-dimensional model along the x-direction in figure 1a, the tangential coupling strength vanishes, or $\boldsymbol{S_w} = (s_w, 0)$. Then, the governing equations can be simplified as

$$\begin{cases} -\imath\omega_0 p = K_w \dfrac{\partial v}{\partial x} - \omega_0^2 s_w v, \\ -\dfrac{\partial p}{\partial x} = \imath\omega_0 s_w \dfrac{\partial v}{\partial x} + \imath\omega_0 \rho_w v. \end{cases} \tag{2.7}$$

The travelling wave inside the Willis unit is assumed to be a plane wave

$$p = p_0 \exp(-\imath k_w x). \tag{2.8}$$

Substituting equation (2.8) into equation (2.7), the wave number k_w can be solved as

$$k_w = \pm\sqrt{\frac{\rho_w}{K_w}}\omega_0, \tag{2.9}$$

where the positive and negative signs correspond to forward and backward travelling waves, respectively. Then, the local velocity can be calculated by equation (2.7) as

$$v = \frac{p}{Z_w^+}, \qquad k_w > 0, \tag{2.10a}$$

and

$$v = \frac{p}{Z_w^-}, \qquad k_w < 0, \tag{2.10b}$$

and the corresponding characteristic impedances are

$$Z_w^+ = -\imath\omega_0 s_w + Z_w^0, \quad k_w > 0, \tag{2.11a}$$

and

$$Z_w^- = -\imath\omega_0 s_w - Z_w^0, \quad k_w < 0, \tag{2.11b}$$

where

$$Z_w^0 = \sqrt{\rho_w K_w}. \tag{2.12}$$

The forward and backward characteristic impedances of Willis unit are no longer opposite to each other due to the appearance of imaginary parts.

For the convenience of numerical simulation under the finite element method, equation (2.6) needs to be rewritten into a coefficient form partial differential equation (PDE). It should be mentioned that not only the fundamental solution but also the continuity condition on the boundaries need to be preserved. This equation is rewritten as

$$\nabla\cdot\left[\frac{1}{(\omega_0^2 s_w^2/K_w)+\rho_w}\nabla p + \left(\frac{\omega_0^2 s_w}{\omega_0^2 s_w^2 + Z_w^{0^2}}, 0\right)p\right] = -\frac{\omega_0^2}{(\omega_0^2 s_w^2/\rho_w)+K_w}p + \left(\frac{\omega_0^2 s_w}{\omega_0^2 s_w^2 + Z_w^{0^2}}, 0\right)\cdot\nabla p. \tag{2.13}$$

The continuity of boundary conditions at x_1 and x_2 can be inferred to be

$$-\boldsymbol{n}_1\cdot\left(\frac{1}{\rho_A}\nabla p\right)\bigg|_{x_1=0} = -\boldsymbol{n}_1\cdot\left[\frac{1}{(\omega_0^2 s_w^2/K_w)+\rho_w}\nabla p + \left(\frac{\omega_0^2 s_w}{\omega_0^2 s_w^2 + Z_w^{0^2}}, 0\right)p\right]\bigg|_{x_1=0} \tag{2.14a}$$

and

$$-\boldsymbol{n}_2\cdot\left(\frac{1}{\rho_B}\nabla p\right)\bigg|_{x_2=h_0} = -\boldsymbol{n}_2\cdot\left[\frac{1}{(\omega_0^2 s_w^2/K_w)+\rho_w}\nabla p + \left(\frac{\omega_0^2 s_w}{\omega_0^2 s_w^2 + Z_w^{0^2}}, 0\right)p\right]\bigg|_{x_2=h_0}. \tag{2.14b}$$

Combined with equations (2.1) and (2.5), they are actually compatible with the continuity of the normal local velocity

$$-\boldsymbol{n}_1\cdot\boldsymbol{v}_A|_{x_1=0} = -\boldsymbol{n}_1\cdot\boldsymbol{v}_w|_{x_1=0} \tag{2.15a}$$

and

$$-\boldsymbol{n}_2\cdot\boldsymbol{v}_B|_{x_2=h_0} = -\boldsymbol{n}_2\cdot\boldsymbol{v}_w|_{x_2=h_0}. \tag{2.15b}$$

https://royalsocietypublishing.org/journal/rspa Proc. R. Soc. A 482: 20251021

It should be mentioned that the Willis unit is conservative and reciprocal, despite the appearance of an imaginary impedance, which can be verified through its impedance matrix and scattering matrix. For any excitation, the sound pressure and velocity fields inside the Willis unit can be expressed as

$$p = \alpha \exp(-\imath k_w x) + \beta \exp(\imath k_w x) \tag{2.16a}$$

and

$$v = \frac{\alpha}{Z_w^+} \exp(-\imath k_w x) + \frac{\beta}{Z_w^-} \exp(\imath k_w x). \tag{2.16b}$$

The impedance matrix can thus be defined as

$$\begin{aligned}\begin{bmatrix} p|_{x_1=0} \\ p|_{x_2=h_0} \end{bmatrix} &= \mathbf{Z} \begin{bmatrix} -\boldsymbol{n}_1 \cdot \boldsymbol{v}|_{x_1=0} \\ -\boldsymbol{n}_2 \cdot \boldsymbol{v}|_{x_2=h_0} \end{bmatrix} \\ &= \begin{bmatrix} Z_{11} & Z_{12} \\ Z_{21} & Z_{22} \end{bmatrix} \begin{bmatrix} -\boldsymbol{n}_1 \cdot \boldsymbol{v}|_{x_1=0} \\ -\boldsymbol{n}_2 \cdot \boldsymbol{v}|_{x_2=h_0} \end{bmatrix}. \end{aligned} \tag{2.17}$$

The impedance matrix should be independent of the external excitation, i.e. unrelated with amplitudes α and β. Therefore, its components can be obtained using the undetermined coefficient method

$$Z_{11} = \imath X_{11} = \frac{-\imath Z_w^0 \cos(k_w h_0) - \imath \omega_0 s_w}{\sin(k_w h_0)}, \tag{2.18a}$$

$$Z_{12} = \imath X_{12} = \frac{-\imath Z_w^0}{\sin(k_w h_0)}, \tag{2.18b}$$

$$Z_{21} = \imath X_{21} = \frac{-\imath Z_w^0}{\sin(k_w h_0)} \tag{2.18c}$$

and

$$Z_{22} = \imath X_{22} = \frac{-\imath Z_w^0 \cos(k_w h_0) + \imath \omega_0 s_w}{\sin(k_w h_0)}. \tag{2.18d}$$

It is obvious that the impedance matrix is purely imaginary and symmetrical, i.e. conservative and reciprocal, respectively. Moreover, the main diagonal components are not equal due to the presence of the Willis term. There are three degrees of freedom provided by k_w, Z_w and s_w, which enable the possibility of a complete modulation of the impedance matrix. This Willis metamaterial simplifies to a usual material when the coupling term vanishes. In such a case, the achievable impedance matrix is limited.

3. One-dimensional perfect transmission with phase modulation

In order to specify the scattering matrix of the Willis unit, a normalization of the impedance matrix needs to be implemented according to the impedances of media A and B. The normalized impedance matrix can be defined by

$$\begin{bmatrix} \left.\dfrac{p}{\sqrt{Z_A}}\right|_{x_1=0} \\ \left.\dfrac{p}{\sqrt{Z_B}}\right|_{x_2=h_0} \end{bmatrix} = \overline{\mathbf{Z}} \begin{bmatrix} -\boldsymbol{n}_1 \cdot \boldsymbol{v}\sqrt{Z_A}|_{x_1=0} \\ -\boldsymbol{n}_2 \cdot \boldsymbol{v}\sqrt{Z_B}|_{x_2=h_0} \end{bmatrix}, \tag{3.1}$$

where Z_A and Z_B are the characteristic impedances of media A and B. It can be easily solved as

$$\begin{aligned}\overline{\mathbf{Z}} &= \begin{bmatrix} \overline{Z_{11}} & \overline{Z_{12}} \\ \overline{Z_{21}} & \overline{Z_{22}} \end{bmatrix} = \imath \begin{bmatrix} \overline{X_{11}} & \overline{X_{12}} \\ \overline{X_{21}} & \overline{X_{22}} \end{bmatrix} \\ &= \imath \begin{bmatrix} \dfrac{X_{11}}{Z_A} & \dfrac{X_{12}}{\sqrt{Z_A Z_B}} \\ \dfrac{X_{21}}{\sqrt{Z_A Z_B}} & \dfrac{X_{22}}{Z_B} \end{bmatrix}. \end{aligned} \tag{3.2}$$

The scattering matrix is then calculated from the normalized impedance matrix

$$\mathbf{S} = (\overline{\mathbf{Z}} - \mathbf{I})(\overline{\mathbf{Z}} + \mathbf{I}). \tag{3.3}$$

The components of the scattering matrix can thus be expressed as

$$S_{11} = \frac{(\overline{Z_{11}} - 1)(\overline{Z_{22}} + 1) - \overline{Z_{12}Z_{21}}}{(\overline{Z_{11}} + 1)(\overline{Z_{22}} + 1) - \overline{Z_{12}Z_{21}}}, \tag{3.4a}$$

$$S_{12} = \frac{2\overline{Z_{12}}}{(\overline{Z_{11}} + 1)(\overline{Z_{22}} + 1) - \overline{Z_{12}Z_{21}}}, \tag{3.4b}$$

$$S_{21} = \frac{2\overline{Z_{21}}}{(\overline{Z_{11}} + 1)(\overline{Z_{22}} + 1) - \overline{Z_{12}Z_{21}}} \tag{3.4c}$$

and

$$S_{22} = \frac{(\overline{Z_{11}} + 1)(\overline{Z_{22}} - 1) - \overline{Z_{12}Z_{21}}}{(\overline{Z_{11}} + 1)(\overline{Z_{22}} + 1) - \overline{Z_{12}Z_{21}}}. \tag{3.4d}$$

For the transmission model under one-sided excitation depicted in figure 1a, the scattering matrix obeys

$$\begin{bmatrix} \dfrac{p_r^0 \exp(\imath\varphi_r)}{\sqrt{Z_A}} \\ \dfrac{p_t^0 \exp(\imath\varphi_t)}{\sqrt{Z_B}} \end{bmatrix} = \begin{bmatrix} S_{11} & S_{12} \\ S_{21} & S_{22} \end{bmatrix} \begin{bmatrix} \dfrac{p_i^0 \exp(\imath\varphi_i)}{\sqrt{Z_A}} \\ 0 \end{bmatrix}, \tag{3.5}$$

where $p_i^0 \exp(\imath\varphi_i)$, $p_t^0 \exp(\imath\varphi_t)$ and $p_r^0 \exp(\imath\varphi_r)$ are the complex amplitudes of the incident, reflected and transmitted waves. Considering a unitary incident amplitude $p_i^0 \exp(\imath\varphi_i) = 1$, we then have

$$S_{11} = p_r^0 \exp \imath\varphi_r \tag{3.6a}$$

and

$$S_{21} = \sqrt{\frac{Z_A}{Z_B}} p_t^0 \exp \imath\varphi_t. \tag{3.6b}$$

Substituting these equations into equations (3.4*a*) and (3.4*b*) and separating the real and imaginary parts, the solution for the material parameters can be obtained as

$$k_w = \frac{1}{h_0} \arccos\left(\frac{(Z_A + Z_B)\cos\varphi_t + (Z_A - Z_B)p_r^0 \cos(\varphi_r - \varphi_t)}{2\sqrt{Z_A Z_B} p_t^0}\right), \tag{3.7a}$$

$$Z_w^0 = \frac{(Z_A + Z_B)\cos\varphi_t + (Z_A - Z_B)p_r^0 \cos(\varphi_r - \varphi_t)}{2[\sin\varphi_t - p_r^0 \sin(\varphi_r - \varphi_t)]} \tan(k_w h_0) \tag{3.7b}$$

and

$$s_w = \frac{(Z_A - Z_B)\cos\varphi_t - (Z_A + Z_B)p_r^0 \cos(\varphi_r - \varphi_t)}{2\omega_0[\sin\varphi_t - p_r^0 \sin(\varphi_r - \varphi_t)]}. \tag{3.7c}$$

For the situation of no reflection ($p_r^0 = 0, p_t^0 = 1$), the equations above simplify to

$$k_w = \frac{1}{h_0} \arccos\left(\frac{(Z_A + Z_B)\cos\varphi_t}{2\sqrt{Z_A Z_B}}\right), \tag{3.8a}$$

$$Z_w^0 = \frac{(Z_A + Z_B)\cos\varphi_t}{2\sin\varphi_t} \tan(k_w h_0) \tag{3.8b}$$

and

$$s_w = \frac{(Z_A - Z_B)\cos\varphi_t}{2\omega_0 \sin\varphi_t}. \tag{3.8c}$$

It should be mentioned that Z_w^0 and k_w are allowed to be complex simultaneously due to the appearance of the inverse cosine function. The whole system is still passive as long as the impedance matrix equations (2.18*a*)–(2.18*d*) remain purely imaginary. According to equations (2.9) and (2.12), the Willis metamaterial would have both complex mass and bulk

https://royalsocietypublishing.org/journal/rspa *Proc. R. Soc. A* **482**: 20251021

modulus simultaneously. This underlines the exchange of kinetic energy and elastic potential energy within the Willis metamaterial.

A specific example of phase modulation for water–air transmedia transmission is provided here as an intuitive demonstration. Medium A is set as water with bulk modulus $K_A = 2.25 \times 10^9$ Pa and mass density $\rho_A = 1000\,\mathrm{kg\,m^{-3}}$, whereas medium B is set as air with $K_B = 1.39 \times 10^5$ Pa and $\rho_A = 1.18\,\mathrm{kg\,m^{-3}}$. The PDE module of COMSOL multiphysics is used for numerical simulation in this section. Transmedia phase difference modulation covering 0–2π every $\pi/5$ is shown in figure 1b. Each view is a strip with a width of 10 cm, whose left and right boundaries are set to be periodic. In the middle of the strip is the Willis metamaterial defined by equation (2.13) with a length of $h_w = 13$ cm. Below and above it are 1 m long general homogeneous media set as water and air, respectively. A perfectly matched layer with a length of 50 cm is connected to both ends of the model to avoid reflections. The excitation is set as a travelling wave with unitary amplitude along the positive y-direction from the water. The operating frequency is set as $f_0 = 2000$ Hz. All fields are normalized with reference to the real part of their respective characteristic impedance. It can be noticed that all waves are transmitted into air without reflection. The normalized amplitude of the transmission field is 1, which indicates that the power is completely emitted into the air medium. In addition, the phase difference of the transmitted field covers 0–2π, clearly overcoming the locked-phase limitation of conventional impedance matching methods.

4. Two-dimensional perfect beam steering with custom direction

Units with phase-only modulation, however, may not provide perfect manipulation of power flow in two dimensions. Metasurfaces tailored from phase gradients often fail as the beam steering angle increases [42]. Fortunately, acoustic impedance theory fills the gap between this theoretical limit and perfect operation [44,45]. An impedance metasurface can be established according to figure 1c. Two fields, p_A and p_B, are connected through a Willis impedance metasurface located at $y = 0$. Both fields obey the scalar Helmholtz equation (2.2) in media A and B. As a stable passive and lossless connection between the two fields, the metasurface should provide a purely imaginary impedance matrix that can be calculated as

$$\begin{bmatrix} p_A|_{x=0^-} \\ p_B|_{x=0^+} \end{bmatrix} = \imath \begin{bmatrix} X_{11} & X_{12} \\ X_{21} & X_{22} \end{bmatrix} \begin{bmatrix} -\boldsymbol{n}_A \cdot \boldsymbol{v}_A|_{x=0^-} \\ -\boldsymbol{n}_B \cdot \boldsymbol{v}_B|_{x=0^+} \end{bmatrix}. \tag{4.1}$$

For beam steering with incidence angle θ_i and refraction angle θ_t, as shown in figure 1c, the two fields read

$$p_A = p_0 \exp(k_A \cos\theta_i x + k_A \sin\theta_i y) \tag{4.2a}$$

and

$$p_B = Qp_0 \exp(k_B \cos\theta_t x + k_B \sin\theta_t y), \tag{4.2b}$$

where $k_i = \sqrt{\rho_i/K_i}\omega_0 (i = A, B)$ is the wavenumber of the two fields, and Q is the amplitude factor. The conservation of global power flow needs to be satisfied:

$$\int_{x=0} \frac{1}{2}\mathrm{Re}[p_A(-\boldsymbol{n}_1 \cdot \boldsymbol{v}_A^*)]\mathrm{d}S + \int_{x=0} \frac{1}{2}\mathrm{Re}[p_B(-\boldsymbol{n}_2 \cdot \boldsymbol{v}_B^*)]\mathrm{d}S = 0, \tag{4.3}$$

where * denotes the complex conjugate. The amplitude factor can then be solved as

$$Q = \sqrt{\frac{Z_B \cos\theta_i}{Z_A \cos\theta_t}}. \tag{4.4}$$

Combining equations (4.2*a*), (4.2*b*) and (4.4) with equation (4.1), the components of this impedance matrix can be solved as

$$X_{11} = -\frac{Z_A}{\cos\theta_i}\cot\Phi(y), \tag{4.5a}$$

$$X_{12} = -\frac{Z_B}{Q\cos\theta_t}\frac{1}{\sin\Phi(y)}, \tag{4.5b}$$

$$X_{21} = -\frac{QZ_A}{\cos\theta_i}\frac{1}{\sin\Phi(y)} \tag{4.5c}$$

and

$$X_{22} = -\frac{Z_B}{\cos\theta_t}\cot\Phi(y), \tag{4.5d}$$

where

$$\Phi(y) = (k_B\sin\theta_t - k_A\sin\theta_i)y. \tag{4.6}$$

It can be noted that the impedance matrix remains symmetric ($X_{12} = X_{21}$) when equation (4.4) is satisfied. Substituting equations (4.5*a*)–(4.5*d*) into equations (2.18*a*)–(2.18*d*), the material parameters required for beam steering can be solved as

$$k_w = \frac{1}{h_0}\arccos\left(\frac{(Q^2+1)\cos\Phi(y)}{2Q}\right), \tag{4.7a}$$

$$Z_w^0 = \frac{(Q^2+1)Z_A\cot\Phi(y)}{2\cos\theta_i}\tan\left[\arccos\left(\frac{(Q^2+1)\cos\Phi(y)}{2Q}\right)\right] \tag{4.7b}$$

and

$$s_w = (1-Q^2)\frac{Z_A}{2\omega_0\cos\theta_i}\cot\Phi(y). \tag{4.7c}$$

An example with an angle of incidence of $\theta_i = 0$ and a small steering angle of $\theta_t = 33$ is presented as a validation for this transmedia Willis impedance metasurfaces in figure 1d. The width of the metasurface is set as

$$D = \frac{\lambda_a}{\sin\theta_t}, \tag{4.8}$$

where $\lambda_a = (2\pi/\omega_0)\sqrt{K_a/\rho_a}$ is the acoustic wavelength in the air. Then, the total width of the metasurface is $D = 30$ cm. The width of each unit is $D/10$, which is 3 cm in this case. It is less than a quarter of the wavelength in air to ensure the uniqueness of the impedance matrix. There is a gap with a width of $\delta = 0.1$ mm between adjacent units for numerical isolation, which has almost no influence on the transmission coefficient. The upper and lower boundaries are set to be periodic. All other settings are consistent with figure 1b, but the material parameters of the Willis metamaterial are determined according to equations (4.7*a*)–(4.7*c*).

It can be noticed that the composed impedance metasurface can work almost perfectly for $\theta_t = 33^\circ$ as shown in figure 1d. A two-dimensional Fourier transform gives a quantitative evaluation showing that 99.2% of the power flow is allocated in the target direction. No reflections are induced at all. Only 0.8% of the power flow is scattered, which mainly results from the discretization of units.

The performance at larger steering angles is one of the major advantages of impedance metasurfaces. Another example with a larger small twist angle of $\theta_t = 64^\circ$ is presented as a validation for transmedia Willis impedance metasurfaces in figure 1e. The width of the metasurface is set according to equation (4.8). It is discretized into six units with a width of 3.2 cm. The efficiency of beam steering remains satisfactory, with 96.8% of the power flow being correctly controlled. No reflections are excited, and only 3.2% of the power flow is scattered due to relatively sparse dispersion, which validates the compatibility between Willis metamaterials and impedance theory.

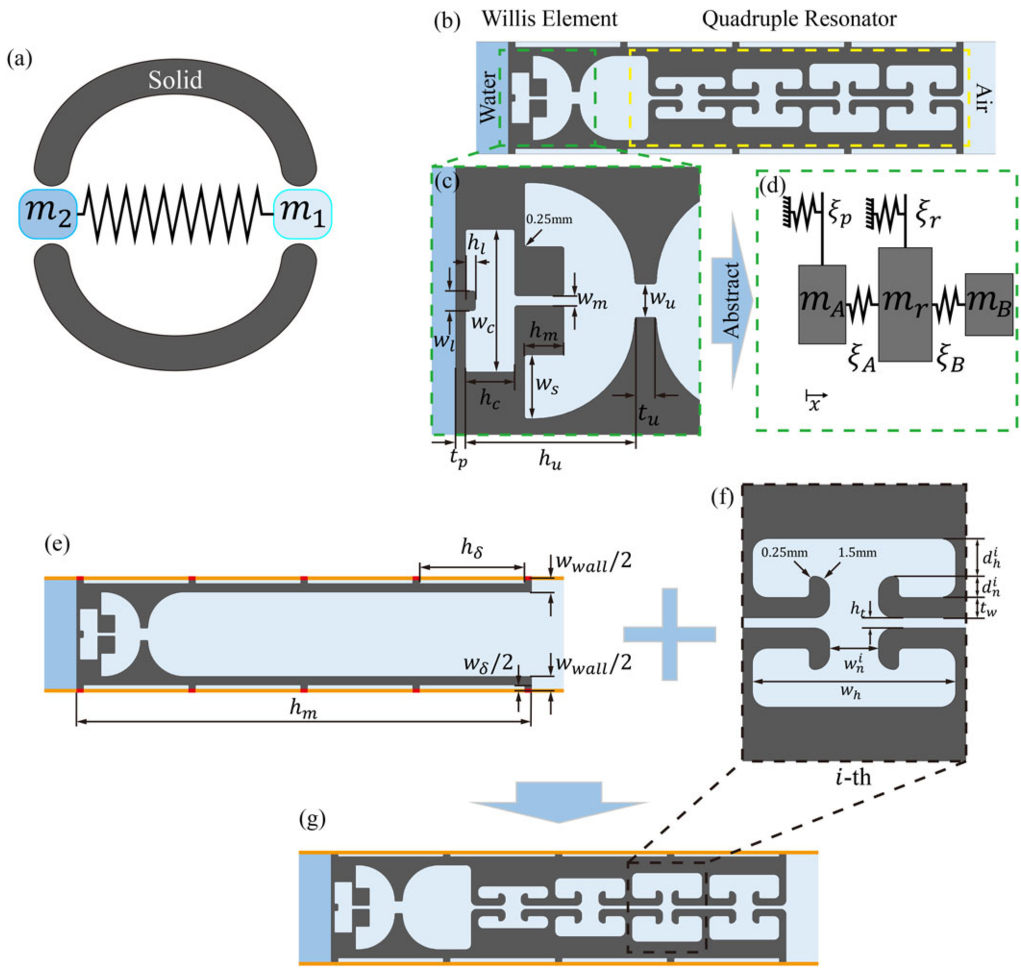

Figure 2. Schematic representation of the hybrid Willis coupling element. (a) Conventional Willis coupling element in homogeneous medium. (b) The overall view of the Willis coupling unit composed of hybrid Willis element and quadruple resonator. (c) Detailed parameters of the Willis coupling element. (d) Mechanical model of the Willis coupling element. (e) The model of the first step optimization for local Willis coupling. (f) Detailed parameters of the second step optimization. (g) The model of the second step optimization for collective response.

5. Design and mechanical analysis of hybrid Willis coupling element

The structure providing Willis coupling in a general homogeneous medium is typically believed to follow the layout shown in figure 2a [36]. The grey area is considered rigid. The fluid mass blocks on both sides of the neck can be regarded as incompressible; the middle fluid cavity can be seen as a spring. Willis coupling is provided when the cross-sectional areas of two necks are asymmetric. However, the topology of this geometry is not directly suitable for application to transmedia transmission. Asymmetry alone, indeed, can hardly support the huge impedance contrast between water and air. The rigid assumption, as well, is no longer applicable to most solids when water is considered. More parameters are furthermore required to cover the target phase difference or the impedance matrix modulation. Moreover, the acoustic-structure interaction between adjacent units needs to be minimized while ensuring that the overall metasurface is not too fragile.

A hybrid Willis coupling unit is therefore proposed herewith along with a two-step parameter optimization procedure, as illustrated in figure 2b–g. The unit, shown in figure 2b, is composed of two parts: a Willis coupling element (green dashed box) and a centrally symmetric quadruple resonator [46,47] (yellow dashed box). The details of a Willis resonance element are depicted in figure 2c. It is composed of a resonant cavity with an open end and a pair of rectangular blocks dividing it in half. On the opposite side of the opening is a thin plate with a mass block in the middle. The air block in the upper opening can be considered incompressible, similar to figure 2a. The thin plate on the left corresponds to the mass block of the other neck in figure 2a. Therefore, the stiffness and the mass of the two mass blocks will be extremely asymmetric, providing a sufficient Willis coupling for transmedia transmission. The pair of mass blocks in the middle are introduced to provide additional degrees of freedom for effective mass and stiffness. The two cavities on their sides can be seen as springs. The mechanical model of the Willis resonance element is abstracted in figure 2d. It includes three mass blocks and four springs. The three masses are denoted as m_A, m_r and m_B from left to right, respectively. The first two springs, corresponding to the two cavities, are denoted ξ_A and ξ_B, respectively. The other two springs are denoted ξ_p and ξ_r; they refer to the elastic connection of the plate and the middle mass blocks on the frame.

The contribution of the parts of the model to effective parameters is examined analytically as follows. The coordinates of the three mass blocks are set as

$$x_A = -a, \quad x_r = e, \quad x_B = a, \tag{5.1}$$

where a is half the total length of the coupled elements and e is the eccentricity. In the long wave limit ($2a/\lambda_a \to 0$), a Taylor's expansion can be applied to describe approximately the displacement of the observable boundary sites. Assuming the effective macroscopic displacement of the frame is u_0, the displacements of the three blocks are

$$u_i = u_0 + \frac{\partial u}{\partial x} x_i, \quad i = A, r, B. \tag{5.2}$$

Without external excitation, the balance of forces applying to the middle mass can be determined as

$$-\xi_r u_r - \xi_A(u_A - u_r) - \xi_B(u_B - u_r) = -\omega_0^2 m_r u_r. \tag{5.3}$$

The apparent pressure and momentum density of the system are defined by [39]

$$p = \frac{1}{2a} \sum_{i=A,B} = f_i x_i \tag{5.4a}$$

and

$$-\imath\omega_0 \mu = \frac{1}{2a} \sum_{i=A,B} = f_i, \tag{5.4b}$$

where f_i is the force exerted on block i. The constitutive relation of this Willis coupling system can be derived by

$$\begin{bmatrix} -\imath\omega_0 p \\ -\imath\omega_0 \mu \end{bmatrix} = \imath \begin{bmatrix} K_{\mathrm{eff}} & \imath\omega_0 s_{\mathrm{eff}} \\ \imath\omega_0 s_{\mathrm{eff}} & \rho_{\mathrm{eff}} \end{bmatrix} \begin{bmatrix} \frac{\partial v}{\partial x} \\ \imath\omega_0 v \end{bmatrix}, \tag{5.5}$$

where $v = \imath\omega_0 u$ and the mass density can be determined by

$$\rho_{\mathrm{eff}} = \frac{m_A + m_B + m_r}{2a}. \tag{5.6}$$

Then, the effective bulk modulus and effective Willis coupling strength can be solved as

$$\begin{aligned} s_{\mathrm{eff}} = &-\frac{1}{2a\omega_0^2}\left[(\xi_A + \xi_p)(a+e) + \xi_B(e-a) - \frac{\xi_p\xi_B(e-a) + \xi_p\xi_A(e+a)}{\omega_0^2 m_r - \xi_r}\right] \\ &- \rho_{\mathrm{eff}}\left[\frac{\xi_B(e-a) + \xi_A(e+a)}{\omega_0^2 m_r - \xi_r} - e\right] \end{aligned} \tag{5.7a}$$

https://royalsocietypublishing.org/journal/rspa *Proc. R. Soc. A* **482**: 20251021

and

$$K_{\rm eff} = -\frac{1}{2}\left[(\xi_A+\xi_p)(a+e)+\xi_B(a-e)-\frac{\xi_p\xi_B(e-a)+\xi_p\xi_A(e+a)}{\omega_0^2 m_r-\xi_r}\right] - \omega_0^2 s_{\rm eff}\left[\frac{\xi_B(e-a)+\xi_A(e+a)}{\omega_0^2 m_r-\xi_r}-e\right]. \tag{5.7b}$$

When different Willis units are connected in parallel, however, vibrations of the elastic part inevitably cause transverse acoustic-structure interaction. In order to take this coupling into account, an optimization procedure is arranged as illustrated in figure 2e–g. To ensure localization of the Willis coupling provided by the solid, multiple rectangular regions filled with air are set on both sides of the unit. Their width and length are set to $w_\delta = 3$ mm and $h_\delta = 30$ mm, respectively. Their role is to ensure that the transverse connection between units is soft enough while at the same time avoiding excessive vertical deformation inside the unit. Parameter optimization for this first step is carried out with the model described by figure 2e. The solution space consists of 11 parameters shown in figure 2c. The total thickness of the unit is set to $h_m = 13$ cm. Its width is determined later from the refraction angle and the discretization. The wall thickness between units is $w_w = 8$ mm. All corners are rounded with a radius of 0.25 mm to avoid singularities in numerical simulations. The solid part is set as an epoxy resin, with Young's modulus $E_m = 3$ GPa, Poisson's ratio $\nu_m = 0.41$, and density $\rho_m = 1140\,\mathrm{kg\,m^{-3}}$. The light blue part is set to air, while the dark blue part is set to water. The upper and lower boundaries (orange line) of the fluid part enforce periodic periodic boundary conditions, whereas the left and right ends are terminated by perfectly matched layers. In the first step, the model is calculated twice with the boundaries of the solid part (red line) either set to periodic or clamped, as shown in figure 2e. The influence of boundary conditions on vibrations of the solid is supposed to be minimal when efficient transmission with the same phase difference is provided under both boundary conditions. Therefore, the fitness value for the first step is defined as

$$f_1 = \frac{1}{2}|S_{12}^{\rm period} + S_{12}^{\rm fix}|. \tag{5.8}$$

Willis coupling can be considered to be localized within the unit when $f_1 = 1$.

The second step of the optimization procedure is carried out after introducing the resonators with parameters inherited from the first step, as shown in figure 2f,g. Then, the Willis coupling elements with significant acoustic-structure interaction are identical for each unit in the metasurface. The transverse imbalance could potentially be reduced to a minimum. Moreover, the quadruple resonator is imposed to be centrally symmetric as well. Differing from its application in airborne acoustics [46], the acoustic-structure interaction cannot be ignored when water serves as one of the acoustic media. With a symmetrical design, the imbalance caused by air resonance can be avoided as much as possible. Rounded corners with radius 1.5 mm are also considered in the most easily bendable parts. The upper and lower boundaries (orange line) of solid and fluid parts all receive periodic boundary conditions. The parameters in figure 2f are used to optimize the collective response of the unit in order to approach the target interface impedance matrix. The fitness value for the second step is defined as

$$f_2 = ||\overline{\mathbf{Z}}^{\rm opt} - \overline{\mathbf{Z}}^{\rm tar}||. \tag{5.9}$$

The optimized samples are considered satisfactory when f_2 approaches 0. As a consequence, the impedance matrix of each unit is collectively contributed by both the Willis element and the quadruple resonator.

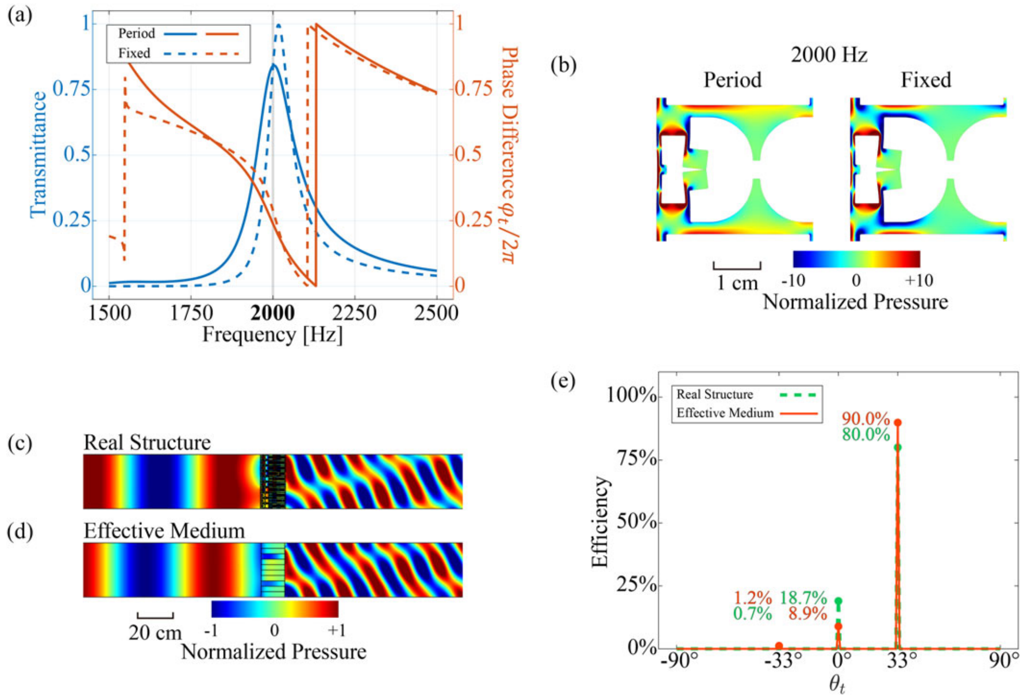

Figure 3. Numerical simulation of impedance metasurfaces with a small angle of refraction of 33°. (a) Transmission characteristics of a hybrid Willis coupling element with width $w_u = 3$ cm. (b) Vibration modes of the Willis coupling element under periodic and fixed boundary conditions, at 2000 Hz. (c) Response of an optimized metasurface. (d) Response of the same metasurface considering the effective parameters retrieved from optimization. (e) Quantitative evaluation provided by two-dimensional Fourier transform.

6. Transmedia Willis impedance metasurface with minimal acoustic-structure interaction

In this section, two metasurfaces corresponding to the two examples discussed in §4 are designed by the optimization procedure proposed in §5. Numerical results for the model with real structures in this section are given using the solid mechanics and acoustics modules of COMSOL multiphysics. The first metasurface is designed for beam steering with $\theta_t = 33°$. The total width of the metasurface is $D = 30$ cm; it is discretized into 10 units with width $w_u = 3.0$ cm. The transmittance (blue curve) and the phase difference (orange curve) of the wave transmitted by the Willis coupling element optimized in the first step are plotted in figure 3a under both periodic (solid curve) and fixed (dashed curve) boundary conditions. Detailed parameters and process of the two-step optimization are provided in appendix A. It can be noted that both curves coincide around the operating frequency with a high transmittance owing to the fitness function equation (5.8). The difference caused by the boundary conditions in transmission characteristics is minimized as much as possible. The vibration modes observed under both boundary conditions at the operating frequency are shown in figure 3b. Deformations are basically consistent with each other, as expected. Only the plate that is in contact with water and the central mass block vibrates, whereas the frame remains stationary. The pressure field inside the solid part is extracted to evaluate the locality of vibration. The pressure is concentrated near the plate and the mass block, with only a small fraction spreading to the boundary.

The units obtained after the second optimization step are connected in parallel to form a metasurface, whose operating performance is depicted in figure 3c. Detailed parameters are provided in appendix A. The pressure distribution visually matches the target performance shown in figure 2b, though with more scattering. Some reflections in water can be noticed in the sound field, especially near the metasurface. This collective phenomenon is contributed to not only by unit discretization but also by deviations introduced by optimization and by acoustic-structure interaction. In order to evaluate the impact of the transverse acoustic-structure interaction, the effective parameters retrieved from the optimized structure are used for the numerical simulation of figure 3d with the PDE model. Then, the remaining scattering can be considered to be mostly caused by deviations introduced by optimization. The difference between figure 3c and figure 3d is mainly due to structural vibrations that somewhat mitigate the operation of the metasurface. A quantitative evaluation is provided in figure 3e by a two-dimensional Fourier transform of the pressure field. Compared to the theoretical limit value of 99.2% in figure 2b, the deviation introduced by parameter optimization leads to a decreased efficiency of 90.0%. Residual transverse acoustic-structure interaction furthermore results in an additional 10.0% reduction.

Transverse acoustic-structure interaction may be even more stringent for localization within the metasurface unit in the case of beam steering with a larger angle of refraction of 64°. Nonetheless, it can still be achieved by the proposed Willis metasurface and two-step optimization procedure. The total width of the metasurface is $D = 19.2\,\text{cm}$ according to equation (4.8); it is discretized into six units with width $w_u = 3.2\,\text{cm}$. The unit is slightly wider than the former one in order to weaken the acoustic-structure interaction. Repeating the above optimization process, the parameters of the Willis coupling element are provided in appendix A. The transmittance (blue curve) and the phase difference (orange curve) of the wave transmitted under the two boundary conditions (solid curve for periodic boundary and dashed curve for fix boundary) are plotted in figure 4a. Both curves can be noticed to coincide around the operating frequency. The vibration modes and pressure distribution in the solid are also presented in figure 4b. The two models, though they assume different boundary conditions, share the same vibration mode. The pressure is more concentrated in the middle of the unit than for the former metasurface and has almost not developed to both edges. Transverse interaction can be considered as reduced further due to the widening of the unit. The operation of adjacent units can be seen as almost isolated.

After the second step of optimization, the performance of the composed metasurface is shown in figure 4c; detailed parameters are provided in appendix A. The transmission field is basically the same as the target of figure 2c, with only dim reflections excited. Moreover, numerical simulation using the effective parameters extracted from the optimized structure is given in figure 4d with the PDE module; there are almost no differences compared to figure 4c. It can be read from the quantitative evaluation in figure 4e that the operation performances for figure 4c,d are close, with efficiencies of 92.7% and 90.7%, respectively. Transverse acoustic-structure interaction only causes a reduction of 2% in this case.

It can be noted that there is actually a contradiction between the discretization of units and the localization of acoustic-structure interaction. For the case with a refractive angle smaller than 33°, the period of the metasurface is larger. A denser discretization can be adopted, yielding better theoretical performance of the metasurface as shown in figure 1d. However, more discretized units imply a reduced unit width. The difficulty of localizing the acoustic-structure interaction at such a narrow spatial scale is the main factor limiting the effectiveness of metasurfaces. Differences in boundary conditions still have a noticeable impact on the Willis coupling element as shown in figure 3a,b. The performance of the metasurface is thus weakened as shown in figure 3e. For the case with a refractive angle larger than 64°, discretization must be sparser to accommodate the unit structure design. The theoretical performance of the metasurface is weakened compared to the one with smaller refractive angle as shown in figure 1e. However, its units are set with larger width, facilitating the localization of acoustic-structure interaction within the Willis element. The transverse interaction is significantly reduced as the two curve pairs nearly coincide as shown in figure 4a. The performance of the composed metasurface also becomes better as shown in figure 4e.

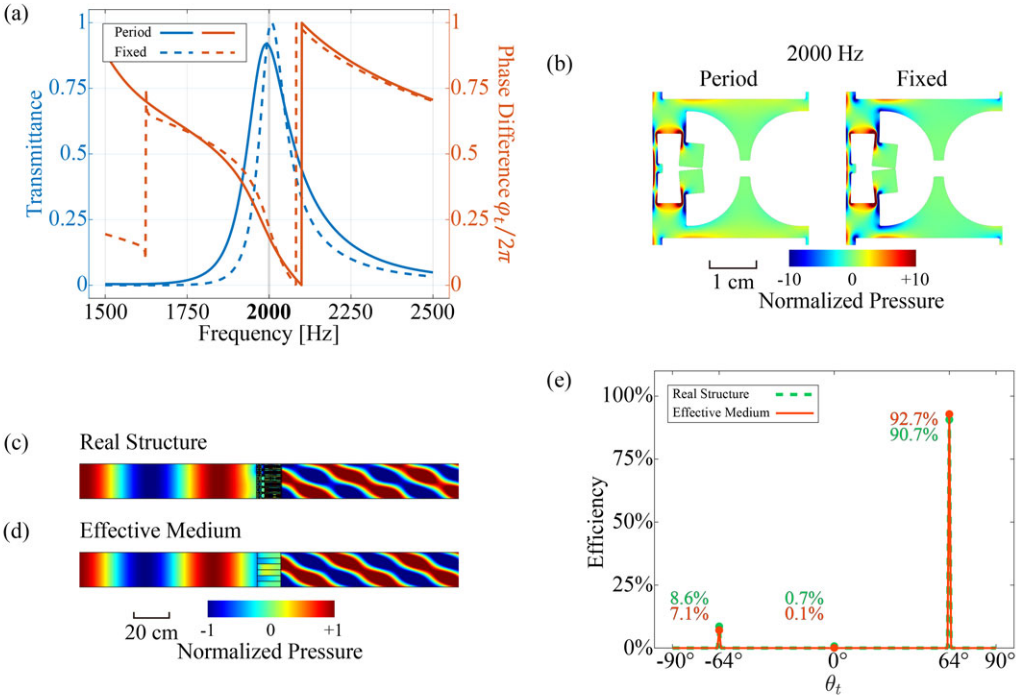

Figure 4. Numerical simulation of impedance metasurfaces with a large angle of refraction of 64°. (a) Transmission characteristics of a hybrid Willis coupling element with width $w_u = 3.2$ cm. (b) Vibration modes of the Willis coupling element under periodic and fixed boundary conditions, at 2000 Hz. (c) Response of an optimized metasurface. (d) Response of the same metasurface considering the effective parameters retrieved from optimization. (e) Quantitative evaluation provided by two-dimensional Fourier transform.

In particular, when the refractive angle approaches $\pi/2$, the period of the metasurface further decreases. The contradiction between the discretization of units and the localization of acoustic-structure interaction becomes more pronounced. Moreover, the presence of the quadruple resonator may become a barrier to broadband operation of Willis impedance metasurfaces. The losses in the resonant cavity will also be significant if viscosity is considered. Discrepancies introduced by fabrication tolerance could degrade the performance for the same reason. A discussion of potential impact of mismatches in operating frequency, viscosity and fabrication tolerance is given in appendix B, taking the metasurface with a larger refractive angle of 64° as an example. Alternative strategies for non-resonant unit structural design should be explored in future work to address these challenges.

7. Conclusion

In this paper, Willis coupling metamaterials are developed for the design of transmedia acoustic metasurfaces. The transmission characteristics and impedance matrix of Willis metamaterial have been systematically analysed, covering the requirements of arbitrary transmedia wave manipulation. A hybrid structure with Willis coupling is proposed as a practical base for the unit design of impedance metasurfaces. A two-step optimization is established to discretize unit design while minimizing the transverse acoustic-structure interaction. Finally, the performances of the composed Willis impedance metasurfaces are validated in simulation.

Willis metamaterials have promising application prospects in metasurface design, particularly for transmedia problems. Not only in acoustics but also Willis coupling in elasticity can provide alternative degrees of freedom from the perspective of constitutive relationships. It possesses both the anomalous wave behaviours provided by conventional metamaterials and the compactness of metasurfaces. The interaction between solid structures and acoustic field may still be the main subject of transmedia metasurface design. Transverse interaction may be further reduced if the metasurface unit is designed to be wider, as demonstrated in this work. However, this would result in sparse discretization or a narrower range of steering angles. A more compact strategy under the framework of acoustic-structure interaction will be pursued in further study. Another disadvantage for such structures is the narrowband operation due to the introduction of resonators. But non-resonant structures like maze-like unit may not be compatible with symmetrical design as the quadruple resonator in this work. Alternative mechanisms for the modulation of the impedance matrix remain to be developed. In addition, only the application of one-dimensional Willis metamaterials in metasurfaces is discussed in this paper. The transverse Willis coupling strength will be non-zero when the unit structure is designed asymmetrically. The composed metasurface will be able to carry transverse power flow transmission subjectively, which may further support the design based on generalized impedance theory. This work will enrich the mechanism for transmedia wave manipulation and the structure design for the unit of transmedia metasurfaces.

Data accessibility. All data are provided in the appendix.

Declaration of AI use. We have not used AI-assisted technologies in creating this article.

Authors' contributions. Y.-Z.T.: conceptualization, data curation, funding acquisition, software, writing—original draft; Y.-F.W.: supervision, funding acquisition, project administration, resources, writing—review and editing; V.L.: formal analysis, resources, writing—review and editing; Y.-S.W.: supervision, writing—review and editing.

All authors gave final approval for publication and agreed to be held accountable for the work performed therein.

Conflict of interest declaration. We declare we have no competing interests.

Funding. This work was supported by the National Natural Science Foundation of China (grant nos. 124B2034 and 12021002). V.L. acknowledges financial support by the EIPHI Graduate School (ANR-17-EURE-0002).

Appendix A. Parameters of the designed hybrid Willis impedance metasurfaces

Detailed parameters for the hybrid elements of the two cases are recorded in the second and third columns of table 1, respectively. Detailed parameters of the quadruple resonators in cases 1 and 2 are recorded in tables 2 and 3, respectively. The parameter spaces for optimization are given in the last column of each table. A genetic algorithm is employed to access the target transmission and impedance matrices. The probabilities of crossover and mutation are both set to 50%. The fitness value is calculated according to equations (5.8) and (5.9). Each model is optimized five times, with 1000 generations and 20 samples per generation. The best samples are used to assemble the final metasurface.

Appendix B. Discussion of the potential impact of mismatches on operating frequency, viscosity and fabrication tolerance

The frequency-domain response for the efficiency of the metasurface with a refractive angle of 64° (Case 2) is shown in figure 5. High efficiency is achieved only near the target operating frequency of 2000 Hz. The quadruple resonators cause significant efficiency fluctuations as the frequency deviates from the design value. Consequently, the metasurface exhibits narrowband filtering characteristics.

The impacts of viscosity in the solid and fluid are investigated in simulations, respectively. For the metasurface at a given operating frequency $f_0 = 2000\,\mathrm{Hz}$, the viscosity in the solid is characterized by a complex Young's modulus

$$E^v = E_m(1 + \imath \tan\delta), \tag{B 1}$$

where $\tan\delta$ is the loss tangent defined as the ratio of the imaginary part to the real part of the modulus. The loss tangent is varied from 0% to 1% to evaluate the impact of viscosity on the performance of the Willis impedance metasurface. The simulation results are plotted as a

Table 1. Parameters optimized in the first step (unit: cm).

	case 1	case 2	parameter space
w_c	1.42	1.45	[0.60,1.50]
h_c	0.50	0.50	[0.30,0.50]
h_m	0.40	0.40	[0.20,0.60]
w_s	0.65	0.65	[0.35,0.80]
w_m	0.10	0.10	[0.10,0.30]
w_u	0.38	0.34	[0.10,0.40]
h_u	2.06	1.87	[1.70,3.00]
t_p	0.10	0.10	[0.10,0.30]
t_u	0.15	0.22	[0.10,0.30]
w_l	0.20	0.20	[0.20,0.50]
h_l	0.10	0.10	[0.10,0.25]

Table 2. Optimized parameters in the second step for the units in case 1 (unit: cm).

unit	1	2	3	4	5	6	7	8	9	10	parameter space
d_h^1	0.21	0.40	0.45	0.16	0.31	0.54	0.21	0.15	0.28	0.19	[0.15, 0.70]
d_n^1	0.53	0.22	0.30	0.42	0.24	0.21	0.29	0.44	0.23	0.18	[0.10, 0.60]
w_n^1	0.43	0.45	0.40	0.48	0.20	0.28	0.45	0.46	0.39	0.20	[0.10, 0.50]
d_h^2	0.30	0.50	0.53	0.25	0.32	0.20	0.44	0.38	0.30	0.57	[0.15, 0.70]
d_n^2	0.20	0.25	0.23	0.35	0.36	0.36	0.15	0.37	0.35	0.18	[0.10, 0.60]
w_n^2	0.18	0.21	0.31	0.29	0.48	0.49	0.15	0.48	0.27	0.23	[0.10, 0.50]
d_h^3	0.38	0.27	0.29	0.26	0.17	0.22	0.16	0.53	0.22	0.17	[0.15, 0.70]
d_n^3	0.30	0.21	0.24	0.27	0.35	0.15	0.55	0.22	0.38	0.54	[0.10, 0.60]
w_n^3	0.18	0.36	0.38	0.44	0.33	0.45	0.48	0.38	0.48	0.41	[0.10, 0.50]
d_h^4	0.32	0.19	0.22	0.26	0.26	0.26	0.18	0.28	0.28	0.20	[0.15, 0.70]
d_n^4	0.19	0.26	0.21	0.15	0.19	0.15	0.27	0.16	0.17	0.25	[0.10, 0.60]
w_n^4	0.40	0.49	0.38	0.24	0.41	0.41	0.39	0.19	0.30	0.20	[0.10, 0.50]
h_t	0.17	0.19	0.17	0.24	0.25	0.24	0.24	0.23	0.18	0.18	[0.10, 0.20]

green solid line in figure 6. The transmission efficiency decreases from 90.7% as the loss tangent increases. Additionally, thermoviscous effects in the fluid are considered by modelling the fluid inside the metasurface using the thermoviscous acoustics module of COMSOL Multiphysics. The efficiency is significantly reduced, as indicated by the blue dashed line in figure 6. With only the thermoviscous effect introduced, the efficiency drops from 90.7% to 27.7%. As the loss tangent increases, the efficiency further decreases as well.

A fabrication error with a maximum value of ± 0.1 mm (i.e. ranging from -0.1 mm to $+0.1$ mm) is assumed to assess the parameter tolerance of the metasurface. Errors are introduced separately into the Willis element and the quadruple resonator. For each case, 1000 random samples are generated using COMSOL multiphysics with MATLAB. Then, the resulting maximum relative error is 10% according to the parameters in tables 1 and 3. The probability density functions of efficiency are shown in figure 7a,b, respectively. Figure 7a shows a distinct peak at an efficiency of

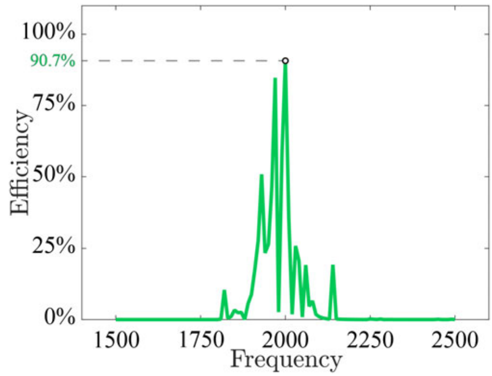

Figure 5. The frequency-domain response for the efficiency of the metasurface with a refractive angle of 64°.

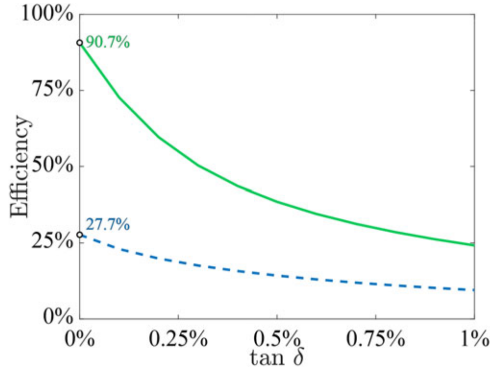

Figure 6. Efficiency of the metasurface with a refractive angle of 64° under viscosity in the solid alone (green solid line) and in both solid and fluid (blue dashed line).

Table 3. Optimized parameters in the second step for the units in case 2 (unit: cm).

unit	1	2	3	4	5	6	parameter space
d_h^1	0.35	0.53	0.20	0.50	0.28	0.28	[0.15, 0.70]
d_n^1	0.38	0.22	0.49	0.25	0.25	0.24	[0.10, 0.60]
w_n^1	0.49	0.23	0.24	0.13	0.29	0.41	[0.10, 0.50]
d_h^2	0.52	0.35	0.39	0.27	0.37	0.43	[0.15, 0.70]
d_n^2	0.23	0.31	0.30	0.47	0.31	0.32	[0.10, 0.60]
w_n^2	0.38	0.30	0.46	0.23	0.21	0.23	[0.10, 0.50]
d_h^3	0.60	0.32	0.50	0.50	0.35	0.36	[0.15, 0.70]
d_n^3	0.15	0.27	0.25	0.25	0.39	0.28	[0.10, 0.60]
w_n^3	0.41	0.27	0.37	0.50	0.38	0.23	[0.10, 0.50]
d_h^4	0.33	0.35	0.34	0.21	0.33	0.22	[0.15, 0.70]
d_n^4	0.32	0.30	0.31	0.38	0.21	0.28	[0.10, 0.60]
w_n^4	0.23	0.20	0.21	0.14	0.43	0.31	[0.10, 0.50]
h_t	0.23	0.25	0.25	0.11	0.24	0.20	[0.10,0.20]

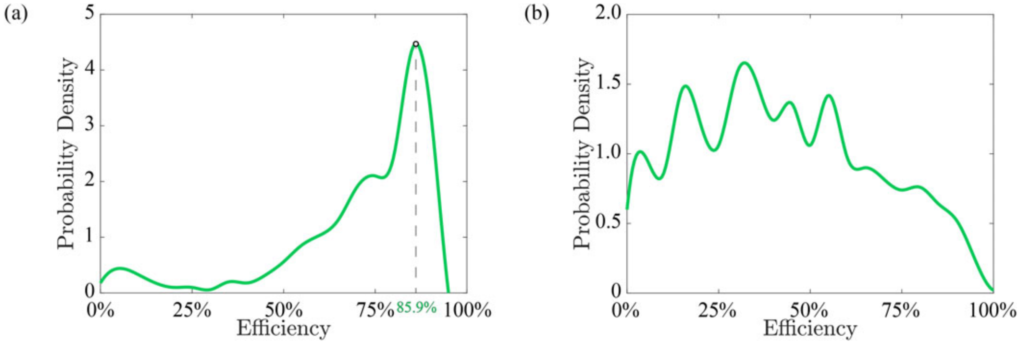

Figure 7. Probability density functions of efficiency for (a) the Willis element and (b) the quadruple resonator under a fabrication error with maximum value of ± 0.1 mm.

85.9%, indicating that the Willis coupling element has some robustness to fabrication errors. The efficiency distribution is nearly uniform when errors are imposed into the quadruple resonator as shown in figure 7b. This indicates high sensitivity to fabrication errors due to the presence of resonators. Future work will focus on developing non-resonant mechanisms to improve robustness against mismatches in operating frequency and fabrication tolerance.

References

1. Qiu T, Zhao Z, Zhang T, Chen C, Chen CLP. 2019 Underwater Internet of Things in smart ocean: system architecture and open issues. *IEEE Trans. Ind. Inf.* **16**, 4297–4307. (doi:10.1109/TII.2019.2946618)
2. Sun Z, Guo H, Akyildiz IF. 2022 High-data-rate long-range underwater communications via acoustic reconfigurable intelligent surfaces. *IEEE Commun. Mag.* **60**, 96–102. (doi:10.1109/MCOM.002.2200058)
3. Godin OA. 2008 Sound transmission through water–air interfaces: new insights into an old problem. *Contemp. Phys.* **49**, 105–123. (doi:10.1080/00107510802090415)
4. Leighton TG. 2012 How can humans, in air, hear sound generated underwater (and can goldfish hear their owners talking)? *J. Acoust. Soc. Am.* **131**, 2539–2542. (doi:10.1121/1.3681137)
5. Pierce AD. 2019 *Acoustics: an introduction to its physical principles and applications*. Berlin: Springer.
6. Assouar B, Liang B, Wu Y, Li Y, Cheng J-C, Jing Y. 2018 Acoustic metasurfaces. *Nat. Rev. Mater.* **3**, 460–472. (doi:10.1038/s41578-018-0061-4)
7. Wang Y-F, Wang Y-Z, Wu B, Chen W, Wang Y-S. 2020 Tunable and active phononic crystals and metamaterials. *Appl. Mech. Rev.* **72**, 040801. (doi:10.1115/1.4046222)
8. Chen A-L, Wang Y-S, Wang Y-F, Zhou H-T, Yuan S-M. 2022 Design of acoustic/elastic phase gradient metasurfaces: principles, functional elements, tunability, and coding. *Appl. Mech. Rev.* **74**, 020801. (doi:10.1115/1.4054629)
9. Bretagne A, Tourin A, Leroy V. 2011 Enhanced and reduced transmission of acoustic waves with bubble meta-screens. *Appl. Phys. Lett.* **99**, 221906. (doi:10.1063/1.3663623)
10. Godin OA. 2006 Anomalous transparency of water–air interface for low-frequency sound. *Phys. Rev. Lett.* **97**, 164301. (doi:10.1103/PhysRevLett.97.164301)
11. Godin OA. 2007 Transmission of low-frequency sound through the water-to-air interface. *Acoust. Phys.* **53**, 305–312. (doi:10.1134/S1063771007030074)
12. Godin OA. 2008 Low-frequency sound transmission through a gas–liquid interface. *J. Acoust. Soc. Am.* **123**, 1866–1879. (doi:10.1121/1.2874631)
13. Cai Z *et al.* 2019 Bubble architectures for locally resonant acoustic metamaterials. *Adv. Funct. Mater.* **29**, 1906984. (doi:10.1002/adfm.201906984)
14. Lee T, Iizuka H. 2020 Sound propagation across the air/water interface by a critically coupled resonant bubble. *Phys. Rev. B* **102**, 104105. (doi:10.1103/PhysRevB.102.104105)
15. Huang Z *et al.* 2021 Tunable fluid-type metasurface for wide-angle and multifrequency water–air acoustic transmission. *Research* **2021**, 9757943.

16. Bakhtiary Yekta H, Norris AN. 2025 Total acoustic transmission between fluids using a solid material with emphasis on the air–water interface. *Proc. A* **481**, 20240461.
17. Bakhtiary Yekta H, Norris AN. 2025 A broadband solid impedance transformer for acoustic transmission between water and air. *J. Sound Vib.* **611**, 119120. (doi:10.1016/j.jsv.2025.119120)
18. Gong X-T, Zhou H-T, Zhang S-C, Wang Y-F, Wang Y-S. 2023 Tunable sound transmission through water–air interface by membrane-sealed bubble metasurface. *Appl. Phys. Lett.* **123**, 231703. (doi:10.1063/5.0171461)
19. Zhang H, Wei Z, Fan L, Qu J, Zhang S-Y. 2016 Tunable sound transmission at an impedance-mismatched fluidic interface assisted by a composite waveguide. *Sci. Rep.* **6**, 34688. (doi:10.1038/srep34688)
20. Bok E, Park JJ, Choi H, Han CK, Wright OB, Lee SH. 2018 Metasurface for water-to-air sound transmission. *Phys. Rev. Lett.* **120**, 044302. (doi:10.1103/PhysRevLett.120.044302)
21. Zhang S-C, Zhou H-T, Gong X-T, Wang Y-F, Wang Y-S. 2024 Discrete metasurface for extreme sound transmission through water–air interface. *J. Sound Vib.* **575**, 118269. (doi:10.1016/j.jsv.2024.118269)
22. Shi L, Zhu T, Du Y-L, Zhou H-T, Tian Y-Z, Wang Y-F, Wang Y-S. 2025 A two-dimensional discrete metasurface for wireless acoustic communication through water–air interface. *Eng. Struct.* **341**, 120611. (doi:10.1016/j.engstruct.2025.120611)
23. Liu J, Li Z, Liang B, Cheng J-C, Alù A. 2023 Remote water-to-air eavesdropping with a phase-engineered impedance matching metasurface. *Adv. Mater.* **35**, 2301799. (doi:10.1002/adma.202301799)
24. Zhou H-T, Zhang S-C, Zhu T, Tian Y-Z, Wang Y-F, Wang Y-S. 2023 Hybrid metasurfaces for perfect transmission and customized manipulation of sound across water–air interface. *Adv. Sci.* **10**, 2207181. (doi:10.1002/advs.202207181)
25. Tian Y-Z, Li R, Wang Y-F, Laude V, Wang Y-S. 2024 Transmedia transmission enhancement based on transformation acoustics. *Phys. Rev. B* **110**, 214101. (doi:10.1103/PhysRevB.110.214101)
26. Pendry JB, Schurig D, Smith DR. 2006 Controlling electromagnetic fields. *Science* **312**, 1780–1782. (doi:10.1126/science.1125907)
27. Leonhardt U. 2006 Optical conformal mapping. *Science* **312**, 1777–1780. (doi:10.1126/science.1126493)
28. Chen H, Chan CT. 2010 Acoustic cloaking and transformation acoustics. *J. Phys. D: Appl. Phys.* **43**, 113001. (doi:10.1088/0022-3727/43/11/113001)
29. Milton GW, Briane M, Willis JR. 2006 On cloaking for elasticity and physical equations with a transformation invariant form. *New J. Phys.* **8**, 248. (doi:10.1088/1367-2630/8/10/248)
30. Fan CZ, Gao Y, Huang JP. 2008 Shaped graded materials with an apparent negative thermal conductivity. *Appl. Phys. Lett.* **92**, 251907. (doi:10.1063/1.2951600)
31. Tian Y-Z, Wang Y-F, Huang G-Y, Laude V, Wang Y-S. 2022 Dual-function thermoelastic cloak based on coordinate transformation theory. *Int. J. Heat Mass Transfer* **195**, 123128. (doi:10.1016/j.ijheatmasstransfer.2022.123128)
32. Willis JR. 1981 Variational principles for dynamic problems for inhomogeneous elastic media. *Wave Motion* **3**, 1–11. (doi:10.1016/0165-2125(81)90008-1)
33. Nassar H, He Q-C, Auffray N. 2015 Willis elastodynamic homogenization theory revisited for periodic media. *J. Mech. Phys. Solids* **77**, 158–178. (doi:10.1016/j.jmps.2014.12.011)
34. Nassar H, Xu XC, Norris AN, Huang GL. 2017 Modulated phononic crystals: non-reciprocal wave propagation and Willis materials. *J. Mech. Phys. Solids* **101**, 10–29. (doi:10.1016/j.jmps.2017.01.010)
35. Muhlestein MB, Sieck CF, Wilson PS, Haberman MR. 2017 Experimental evidence of Willis coupling in a one-dimensional effective material element. *Nat. Commun.* **8**, 15625. (doi:10.1038/ncomms15625)
36. Melnikov A, Chiang YK, Quan L, Oberst S, Alù A, Marburg S, Powell D. 2019 Acoustic meta-atom with experimentally verified maximum Willis coupling. *Nat. Commun.* **10**, 3148. (doi:10.1038/s41467-019-10915-5)
37. Li Z, Qu H, Zhang H, Liu X, Hu G. 2022 Interfacial wave between acoustic media with Willis coupling. *Wave Motion* **112**, 102922. (doi:10.1016/j.wavemoti.2022.102922)
38. Milton GW. 2007 New metamaterials with macroscopic behavior outside that of continuum elastodynamics. *New J. Phys.* **9**, 359. (doi:10.1088/1367-2630/9/10/359)
39. Qu H, Liu X, Hu G. 2022 Mass-spring model of elastic media with customizable Willis coupling. *Int. J. Mech. Sci.* **224**, 107325. (doi:10.1016/j.ijmecsci.2022.107325)

40. Cummer SA, Schurig D. 2007 One path to acoustic cloaking. *New J. Phys.* **9**, 45. (doi:10.1088/1367-2630/9/3/045)
41. Chen H, Chan CT. 2007 Acoustic cloaking in three dimensions using acoustic metamaterials. *Appl. Phys. Lett.* **91**, 183518. (doi:10.1063/1.2803315)
42. Díaz-Rubio A, Tretyakov SA. 2017 Acoustic metasurfaces for scattering-free anomalous reflection and refraction. *Phys. Rev. B* **96**, 125409.
43. Li Z, Han P, Hu G. 2024 Willis dynamic homogenization method for acoustic metamaterials based on multiple scattering theory. *J. Mech. Phys. Solids* **189**, 105692. (doi:10.1016/j.jmps.2024.105692)
44. Tian Y-Z, Wang Y-F, Laude V, Wang Y-S. 2024 Generalized acoustic impedance metasurface. *Commun. Phys.* **7**, 34. (doi:10.1038/s42005-024-01529-5)
45. Tian Y-Z, Wei Z-R, Wang Y-F, Laude V, Wang Y-S. 2024 Adjustable phase-amplitude-phase acoustic metasurface for the implementation of arbitrary impedance matrices. *Research* **7**, 0502. (doi:10.34133/research.0502)
46. Li J, Shen C, Díaz-Rubio A, Tretyakov SA, Cummer SA. 2018 Systematic design and experimental demonstration of bianisotropic metasurfaces for scattering-free manipulation of acoustic wavefronts. *Nat. Commun.* **9**, 1342. (doi:10.1038/s41467-018-03778-9)
47. Tian Y-Z, Tang X-L, Wang Y-F, Laude V, Wang Y-S. 2023 Annular acoustic impedance metasurfaces for encrypted information storage. *Phys. Rev. Appl.* **20**, 044053. (doi:10.1103/PhysRevApplied.20.044053)